



LETTER

OPEN ACCESS

RECEIVED

19 October 2022

REVISED

23 February 2023

ACCEPTED FOR PUBLICATION

7 March 2023

PUBLISHED

21 March 2023

Original content from this work may be used under the terms of the [Creative Commons Attribution 4.0 licence](#).

Any further distribution of this work must maintain attribution to the author(s) and the title of the work, journal citation and DOI.



Low resistance electrical contacts to few-layered MoS₂ by local pressurization

Yolanda Manzanares-Negro¹, Jiamin Quan², Maedeh Rassekh^{1,3}, Mohammed Moaied^{1,4} , Xiaoqin Li², Pablo Ares^{1,5,6} , Juan José Palacios^{1,5,6} , Julio Gomez-Herrero^{1,5,6} and Cristina Gomez-Navarro^{1,5,6,*}

¹ Departamento de Física de la Materia Condensada, Universidad Autónoma de Madrid, Cantoblanco 28049, Spain

² Department of Physics, University of Texas at Austin, 78712 Austin, TX, United States of America

³ Department of Physics, University of Guilan, 41335-1914 Rasht, Iran

⁴ Department of Physics, Faculty of Science, Zagazig University, 44519 Zagazig, Egypt

⁵ Condensed Matter Physics Center (IFIMAC), Universidad Autónoma de Madrid, Cantoblanco 28049, Spain

⁶ Instituto Nicolás Cabrera (INC), Universidad Autónoma de Madrid, Cantoblanco 28049, Spain

* Author to whom any correspondence should be addressed.

E-mail: cristina.gomez@uam.es

Keywords: 2D materials, electrical contacts, MoS₂, pressurization, strain engineering

Supplementary material for this article is available [online](#)

Abstract

The performance of electronic and optoelectronic devices is dominated by charge carrier injection through the metal–semiconductor contacts. Therefore, creating low-resistance electrical contacts is one of the most critical challenges in the development of devices based on new materials, particularly in the case of two-dimensional semiconductors. Herein, we report a strategy to reduce the contact resistance of MoS₂ via local pressurization. We fabricated electrical contacts using an atomic force microscopy tip and applied variable pressure ranging from 0 to 25 GPa. By measuring the transverse electronic transport properties, we show that MoS₂ undergoes a reversible semiconducting-metallic transition under pressure. Planar devices in field effect configuration with electrical contacts performed at pressures above ~15 GPa show up to 30-fold reduced contact resistance and up to 25-fold improved field-effect mobility when compared to those measured at low pressure. Theoretical simulations show that this enhanced performance is due to improved charge injection to the MoS₂ semiconductor channel through the metallic MoS₂ phase obtained by pressurization. Our results suggest a novel strategy for realizing improved contacts to MoS₂ devices by local pressurization and for exploring emergent phenomena under mechano-electric modulation.

1. Introduction

In semiconductor devices the output performance is dominated by both a change of resistance at the channel or the contact junctions. Therefore, controlling the charge injection through the electrical contacts is as essential as controlling the semiconductor channel itself. Moreover, the realization of well-controlled low resistance electrical contacts is one of the main challenges to overcome for emerging materials. Atomically thin transition metal dichalcogenides (TMDs), such as MoS₂, are currently among the best alternatives to silicon-based electronics. However, the realization of controlled electrical contacts at the semiconductor-metal interface is yet

an unsolved issue and hinders the reliable performance of TMD-based devices [1, 2].

Few-layered thick MoS₂ combines unique electronic and mechanical properties that make it an appealing semiconductor channel for flexible electronics [3, 4]. Indeed, field-effect transistors based on few-layered MoS₂ have shown large on/off ratios, high charge carrier mobility, and outstanding electrostatic gate coupling due to its atomic thickness. However, analysis of the literature reveals a large variation in device performance due to differences in sample preparation and measurement protocols but also largely due to poorly controlled contacts [5–8].

Up to date, mainly two strategies have succeeded in creating ohmic contacts to MoS₂: the first

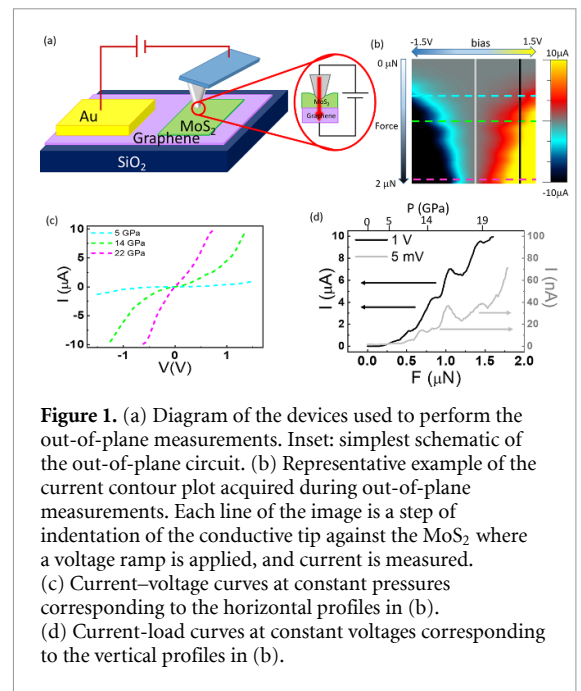
involves the use of semimetals such as graphene [9–14] or bismuth [2] as electrical contacts. These semimetals suppress the appearance of undesirable metal-induced gap states that typically pin the Fermi level in the middle of the gap and make the appearance of Schottky barriers unavoidable. The second strategy is based on chemical phase engineering through locally inducing metallic crystallographic 1 T phase contacts [15, 16]. As the 1 T metallic phase is a metallic version of the channel material, structural atomic mismatch is reduced in these junctions and injection of carriers is facilitated.

Herein we investigate a new approach to create low resistance contacts to few-layered MoS₂ based on local pressurization. Pressurization is a compelling strategy to control the properties of a material, especially for 2D materials where the surface to volume ratio spans several orders or magnitude [17, 18]. Indeed, MoS₂ has been shown to undergo an isostructural semiconducting to metallic transition upon application of high pressures [19–22]. A very efficient strategy to induce and study pressure-induced phenomena at the nanoscale is using an atomic force microscopy (AFM) tip [23–28]. Due to its nanoscale curvature radius, the AFM tip generates a highly concentrated local stress that can reach several GPa.

We show the possibility of inducing a reversible local metallization in MoS₂ under the pressure applied by an AFM tip and subsequently explore the use of this induced metallic phase to perform improved electrical contacts to few-layered MoS₂. We characterized the devices in two different geometries: transverse vertical junctions (figure 1(a)), where we observed local metallization of the semiconductor 2H MoS₂ phase at pressures above 10 GPa. We also used planar devices (several μm in length) contacted through a tip-pressurized junction, where we obtained an improved contact resistance (up to 33 times lower) and enhanced mobility (up to $\times 25$) when the pressure at the contact junction was above 15 GPa. Density functional theory (DFT) based calculations corroborate the metallization of MoS₂ under pressure and the formation of a highly transparent electronic contact between the compressed and the pressure-free phase.

2. Results and discussion

We briefly describe the device fabrication process: for the vertical devices, MoS₂ and graphene bilayers were mechanically exfoliated from bulk crystals onto a polydimethylsiloxane sheet [29, 30] and then transferred to a 300 nm SiO₂/Si substrate (see section 4 materials and methods for details). The stacked samples were annealed under ultrahigh vacuum at 200 °C for 8 h. The graphene bilayers acted as drain electrodes making good electrical contacts to MoS₂ [9] and providing a smooth substrate able



to sustain ultra-high pressures [27]. Then graphene was contacted laterally by shadow masking evaporated top gold electrodes to connect an external macroscopic circuit. Measurements were performed with a homemade AFM in ambient conditions controlled by WSxM software [31] using commercial AFM doped-diamond tips [32]. For these experiments, clean and wrinkle-free areas were selected. The tip was approached to the sample until mechanical contact was established. After that, the tip was further displaced perpendicular to the sample to linearly increase the load on the junction while the cantilever deflection was measured and current vs. bias voltage (*IV*) curves were acquired at each displacement step. To estimate the tip-sample pressure in the experiments we first determined the tip radius using a calibration sample and then we applied the Hertz contact mechanics model [33] as described in SI1. The tip radius was checked before and after each experiment.

Figure 1(b) depicts representative data on a MoS₂ bilayer. It shows a colored two-dimensional contour plot of the current flowing through the vertical device as a function of the bias voltage *V* (horizontal axis) and tip load *F* (vertical axis) *I* (*V*, *F*). As the tip loads the surface, it applies a normal force $F = -k \cdot Z$, where *k* is the cantilever stiffness (calibrated prior experiments) and *Z* the sample perpendicular direction. While *IV* curves at low loads exhibited a semiconductor type behavior consistent with previous works [34, 35], the *IV* curves evolve to linear dependence at high loads, consistent with a metallic phase. We checked the reliability of our electrical contacts by performing similar experiments in the nearby graphene surface where linear *IV*s were obtained at pressures under 5 GPa (see SI2 for further information). Representative horizontal and vertical line cuts

from the 2D contour plot are shown in figures 1(c) and (d) respectively. From figure 1(c), we extracted the conductance at 0 bias voltage as a function of the applied force/pressure, and figure 1(d) shows the plot corresponding to the data of the vertical gray lines drawn in figure 1(b). In thin samples ($N < 5$), for pressures higher than 12 GPa the observed gap eventually disappears. For 18 GPa the conductance at 0 V strongly increases and reaches several $\mu\text{A/V}$ and nearly linear behavior, indicating a semiconductor to metallic conversion in the junction while increasing the pressure exerted by the tip. For N-layered samples with $N > 6$, the MoS_2 fractured before metallization. Fracture of the MoS_2 sample was detected in some experiments as an abrupt step in the *force vs. Z* and *current vs. Z* curves as well as holes and material accumulation in posterior topographies. In this work, we discarded fractured samples, therefore our discussion is limited to those samples showing no damage in our AFM images after the application of pressure (see SI3 for AFM images of undamaged and fractured samples). The experiments showed a similar trend for 1, 2, 3, and 4-layered MoS_2 devices. Data on monolayers and multilayers are depicted in SI4 as examples. We performed our measurements in both loading and unloading directions showing a reversible behavior (SI5 presents an example of an unloading measurement similar to the loading experiment shown in figure 1). Previous works have reported an iso-structural electronic transition in bulk MoS_2 at high pressures that involves full metallization of bulk samples [19, 22, 36]. However, this metallization had never been achieved by local pressurization as shown here. The symmetry of the IV curves, absence of rectifying behavior and lack of current saturation supports that the performance of these devices is dominated by the intrinsic properties of the MoS_2 layers rather than by the metal- MoS_2 junction. Furthermore, our study provides strong evidence that the metallization of few ($N < 5$) layered MoS_2 can be achieved not only by hydrostatic pressure, as reported before, but also under very local pressure as described here.

In figure 2(a) we show the energy gap obtained from our measurements as a function of the applied pressure (continuous lines). Our experimental data are here depicted together with the band gap calculated from DFT calculations under pressure for single, bi-, tri-layer, and bulk systems (see section 4). Our DFT calculations corroborate previous findings revealing that MoS_2 undergoes a semiconducting to metallic transition as a precursor of the 2Hc–2Ha structural transition (see SI6). While the electronic transition is usually completed at 15–20 GPa, the structural 2Hc–2Ha transition occurs at higher pressures. Indeed, both phases undertake a closure of the electronic band gap with applied pressures and have been shown to coexist up to 50 GPa [37]. Qualitatively, both experimental and theoretical gaps follow the same trend, closing at similar pressure values.

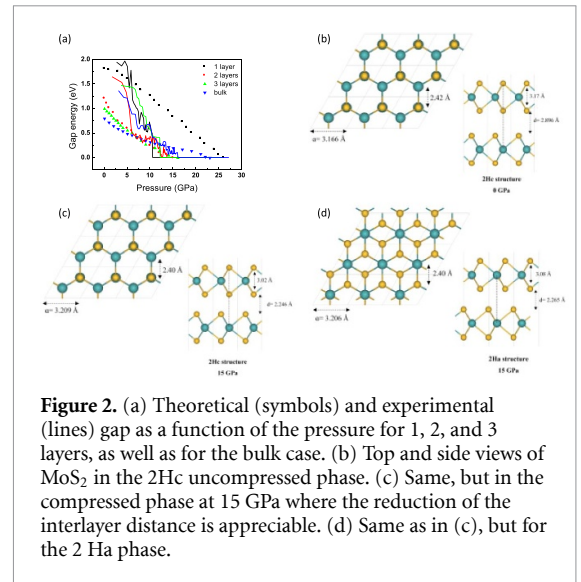
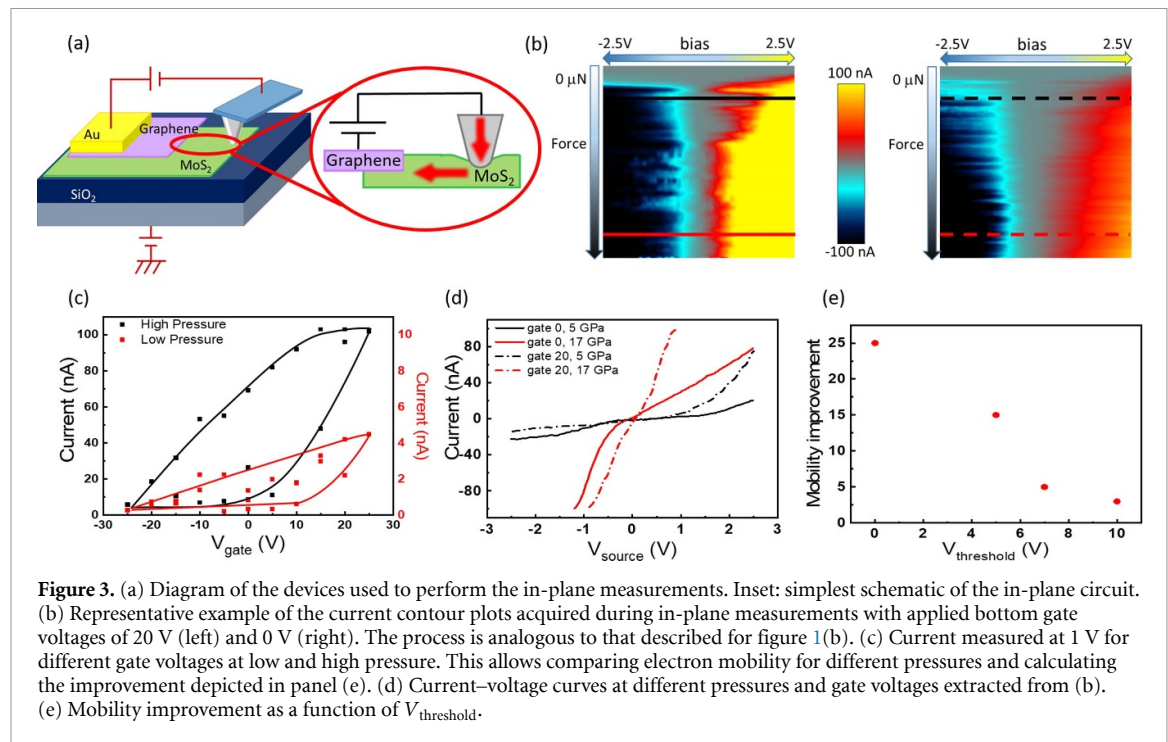


Figure 2. (a) Theoretical (symbols) and experimental (lines) gap as a function of the pressure for 1, 2, and 3 layers, as well as for the bulk case. (b) Top and side views of MoS_2 in the 2Hc uncompressed phase. (c) Same, but in the compressed phase at 15 GPa where the reduction of the interlayer distance is appreciable. (d) Same as in (c), but for the 2Ha phase.

The calculated gap here belongs to the 2Hc structural phase (shown in figure 2(b) for zero pressure and figure 2(c) for high pressure) which is the ground state up to approximately 7 GPa for the bilayer, although it remains being a metastable phase beyond 20 GPa, a value of pressure that we do not reach in the experiments carried out here. At this ultra-high pressure, the energy barrier separating the 2Hc phase from the 2Ha phase [22] vanishes (see SI6). This latter phase is shown in figure 2(d). Interestingly, the electronic gaps of both phases are fairly similar at any pressure evidencing that no structural transition is needed to deliver the semiconducting-metallic conversion.

With the idea of mimicking the approach used by modern silicon microelectronics where contacts are performed by degenerately doped silicon, we explored the possibility of creating improved electrical contacts in planar devices by locally pressurizing the area under a metallic tip acting as an electrode. According to the above-described results, at high pressures the ultimate electrical contact to MoS_2 would be performed through the metallized MoS_2 phase, thus reducing structural mismatch, and facilitating charge carrier injection. Therefore, we prepared samples where the MoS_2 flakes rested on SiO_2 and were placed in contact with graphene-gold contacts on one side (see figure 3(a) for a diagram). Then we measured the current flowing through these planar devices contacting the free MoS_2 edge with a tip pressurized junction while varying the tip load on the junction. In contrast to the transverse setup, this configuration allows applying a bottom gate voltage to our devices. Field effect mobility was evaluated using $\mu = Lg/WC_iV$ where L is the length of the device (distance between the micrometer sized electrode and the AFM tip), g is the derivative of the current with respect to the gate voltage at a certain bias voltage, W is the width of the device, C_i is the capacitance of the



insulating substrate and V is the bias voltage. In order to compare our tip-planar electrode geometry with typical planar-planar electrode geometry, an effective W was calculated for each geometrical configuration using COMSOL Multiphysics as described in section 4.

Our results reveal that devices contacted at low pressure ($P < 5$ GPa) show dominant n-type charge carriers, mobility values between $0.3\text{--}5\text{ cm}^2\text{ s}^{-1}\text{ V}^{-1}$ and a $V_{\text{threshold}}$ ranging from -5 to 10 V. Analogously to figure 1(b), figure 3(b) presents, in a color scale contour plot, electrical current values with varying bias voltage and pressure exerted on the contact in a bilayer device. Representative values for the current at $V_D = 1$ V and varying gate voltage in a bilayer device are shown in figure 3(c). The hysteresis observed in the transfer characteristic in these devices is similar to that reported in previous works and ascribed to the absorption of moisture on the surface and high photosensitivity of MoS_2 [38]. Upon pressure increase, measurements performed at negative gate voltages showed a moderate decrease in the resistance (figure 3(d)). In contrast, measurements performed at positive gate voltages and pressures above 15 GPa exhibited a decreased contact resistance with up to a 30-fold improvement and reached mobility values of $22\text{ cm}^2\text{ s}^{-1}\text{ V}^{-1}$. Table 1 gathers the data obtained in different samples and span from 2 to a 30-fold increase. Interestingly, our data show that this mobility enhancement depends linearly on $V_{\text{threshold}}$ as depicted in figure 3(e). This mobility improvement is larger than that reported by other routes to improve contact resistance such as intercalating different TMDs [39] or chemical methods to remove

Table 1. Comparison of the mobility and contact resistance of four horizontal devices contacted with an AFM conductive tip applying low and ultra-high pressure.

Comparison of planar devices				
Mobility ($\text{cm}^2\text{ V}^{-1}\text{ s}^{-1}$) low pressure	0.35	4.5	0.45	4.95
Mobility ($\text{cm}^2\text{ V}^{-1}\text{ s}^{-1}$) high pressure	9	22.5	6.75	15
Resistance ($\text{M}\Omega$) low pressure	333	38.9	250	21
Resistance ($\text{M}\Omega$) high pressure	10	10	9.7	10
Mobility ratio	25	5	15	3
Resistance ratio	33	4	26	2
$V_{\text{threshold}}$ (V)	0	7	5	10

oxides [40] and the reached mobilities are in the upper 20% for supported bilayer devices [14, 15, 41]. On top of that, the observed improvements of the device's performance at high pressure are comparable to that reported by contacting MoS_2 devices with the 1T metallic phase obtained by chemical routes [15, 16] and suggests that the similarity in atomic structure and band energy level favors electron injection through the pressurized MoS_2 phase. However, the total resistance of our devices is still higher than that reported previously [42, 43]. Our preliminary attempts to estimate contact resistances by the transfer length method and two tip-pressurized contacts (SI7) suggest that this resistance is mainly dominated by a poor graphene- MoS_2 contact that could be further improved.

To gain more insight into the experimental results we performed DFT-based quantum transport calculations (see section 4) of the contact electronic transmission between the pressure-free MoS_2 phase and the compressed one (figures 4(a) and (b)). For

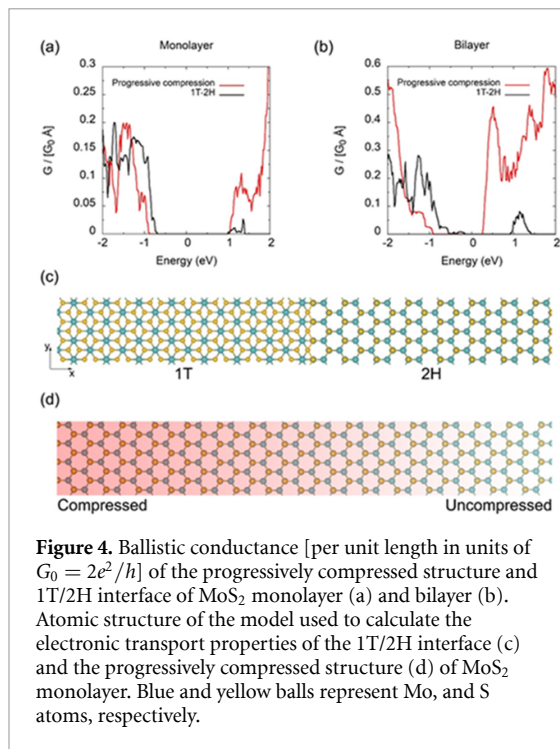


Figure 4. Ballistic conductance [per unit length in units of $G_0 = 2e^2/h$] of the progressively compressed structure and 1T/2H interface of MoS₂ monolayer (a) and bilayer (b). Atomic structure of the model used to calculate the electronic transport properties of the 1T/2H interface (c) and the progressively compressed structure (d) of MoS₂ monolayer. Blue and yellow balls represent Mo, and S atoms, respectively.

comparison purposes, we also considered the case of a 1T/2H interface (where ohmic contacts have already been reported) [15] as shown in figure 4(c). To make it as realistic as possible, we have considered an adiabatically smooth transition between the compressed and pressure-free phases (see figure 4(d)), as expected from the experiments where the pressure must decrease monotonically away from the tip-sample contact center. For computational reasons, here we only take into account the compression effects on the lattice in the transport direction, maintaining the lattice parameters constant in the transversal one. The transmission for both types of contact interfaces is plotted in figures 4(a) and (b) for the monolayer and bilayer cases, respectively. One can appreciate the much higher transmission for the adiabatic compression/pressure-free interface than for the 1T/2H interface, in particular for the case of bilayer devices. In our proposed set up both the reduction of the Schottky barrier and the high transparency conspire to reduce the contact resistance much more effectively than in the 1T/2H interface case. Interestingly, the transmission is even larger for the case of electrons, in agreement with the experimental observation of enhanced mobility for unintentionally *n*-doped samples.

3. Conclusion

In summary, our work demonstrates that the metallic pressurized phase of MoS₂ acts as a very effective contact electrode for its semiconductor counterpart. We have experimentally realized such electrical

contacts by pressing MoS₂ with a conductive AFM tip showing that applied pressures larger than 15 GPa improve the performance of the device by substantially reducing the contact resistance and enhancing the mobility. Our work shows that local pressurization of metal-TMD contacts is an effective route to control charge injection in MoS₂ devices and opens the path for pressure-controlled contact electromechanical devices.

4. Materials and methods

4.1. Sample fabrication

For the vertical devices the MoS₂ and graphene layers were mechanically exfoliated from a bulk crystal onto a polydimethylsiloxane sheet [29]. Graphene was first deposited on top of the SiO₂ substrate, and then large flakes of MoS₂ were transferred on top of the graphene. The stacked samples were annealed under ultrahigh vacuum at 200 °C for 8 h. Then graphene was contacted laterally by 50 nm thick top gold electrodes deposited by thermal evaporation in a high vacuum chamber to connect an external macroscopic circuit. A mask was fixed on the samples so the electrodes were in contact with the desired areas. The process for transferring the samples for the transversal measurements was similar, but in a different order: first MoS₂ was transferred on top of the SiO₂ substrate, and then graphene was transferred on top of everything partially covering the MoS₂ flakes. In this case we did not perform the annealing, and the graphene is equally contacted to the external macroscopic circuit with evaporated gold electrodes.

4.2. AFM measurements

Measurements were performed with a homemade AFM in ambient conditions controlled by WSxM software [28] using commercial AFM doped-diamond tips [29]. Topographies of all the samples were taken in non-invasive amplitude modulation mode to identify the thickness of samples and find clean and wrinkle-free areas. In these areas, the tip was stopped at a specific point, and then approached to the sample until mechanical contact was established. After that, the tip was further displaced perpendicularly to the sample to linearly increase the load on the junction while measuring the cantilever deflection. Current vs. bias voltage (IV) curves at each displacement step were obtained. Measurements were taken in both loading and unloading directions.

4.3. Electronic structure calculations

The MoS₂-2H bulk properties were calculated using DFT [44, 45] with the SIESTA code [46, 47]. The weak interaction between layers, where long-range dispersion van der Waals forces play an important role, calls

for an appropriate exchange and correlation energy functional. We used the nonlocal van der Waals density functional (vdW-DF2) in its second version modification done by Cooper (C09) [48]. We applied the van der Waals C09 to the MoS₂-2H systems and compared the electronic band structure systems for the 1×1 unit cells systems with the experimental results to assess the accuracy of the functional. Moreover, we used the double- ζ plus polarization (DZP) to expand the wavefunctions of the valence electrons [49]. We performed the calculations with a variety of linear combination of atomic orbitals LCAO basis sets and found that the DZP produced high-quality results with an energy shift of 30 meV. The mesh cutoff energy for the integration grid was well converged using 450 Ry. A k-grid of $35 \times 35 \times 5$ Monkhorst-Pack was used to sample the Brillouin zone. A vacuum region in the z -direction of at least 25 Å avoids interactions with periodic images. We fully allowed the structure relaxation until the force tolerance of 10^{-2} eV Å⁻¹ was achieved. Next, we sampled the Brillouin zone using the Monkhorst-Pack scheme with a $45 \times 45 \times 5$ k-point grid for atomic and electronic relaxation. We then extracted the electronic band from the energy eigenvalues of 55 points along the high-symmetry path M- Γ -K-M line.

To apply pressure, we reduced the z -coordinate length of the atoms leaving x - and y -coordinates to be relaxed while calculating the energy, force, unit cell, and energy gap at each step. The pressure was calculated by using the relation (Force/Area of the unit cell) in GPa. By increasing the pressure applied perpendicular to the MoS₂-2H systems, the energy gap decreases gradually and reaches zero at a given pressure without a structural phase transition.

4.4. Ballistic transport calculations

We have obtained the conductance using the Landauer expression, $G = 2e^2/hT(\mu)$, where the transmission T at the Fermi level, μ , is computed with the nonequilibrium Green's function formalism [50]

$$T(\mu) = \frac{\sum_k \text{Tr}[\Gamma_L(k, \mu) G(k, \mu) \Gamma_R(k, \mu) G^+(k, \mu)]}{Na}$$

The system is periodic in the lateral direction. Thus, Green's functions, G , and coupling matrices, Γ , depend on k in this direction. The summation over N values of k in the first Brillouin zone divided by the actual width of the system in the lateral direction (Na , with a being the lateral unit cell width), gives the conductance per unit length. Green's functions and coupling matrices are evaluated from DFT calculations obtained with the OpenMX code [51–53] (www.openmx-square.org/) after computing periodic systems where the supercell is shown in figure 4(c) and d. OpenMX is based on the norm-conserving pseudo-potential method with a partial core correction and pseudoatomic orbitals (LCPAO) as basic functions, here specified by Mo(7.0) – s2 p2d1, and S(7.0) – s2

p2d1, where Mo and S are the atomic symbols for Molybdenum and Sulfur, 7.0 is the cutoff radius in units of Bohr, and s2 p2d1 indicates that two primitive orbitals for each of s and p components and one primitive orbital for d components are employed. A vacuum spacing of 30 Å in the z -direction is used to prevent the interaction between periodic images. Cutoff energy of 220 Ry and a $7 \times 7 \times 1$ k-grid have been used in all presented results. The exchange-correlation functional was the GGA-PBE [54]. All calculations were performed until the change in total energy between two successive iteration steps converged to less than 10^{-6} Hartree. For bilayers, van der Waals interaction (vdW) correlation is considered using the semiempirical dispersion-corrected density functional theory (DFT-D2) force-field approach.

4.5. Effective width of the samples for mobility calculation

We used COMSOL Multiphysics to simulate every measured geometry to estimate the effective width of the device. To do so, we simulated a MoS₂ strip of 5 μ m in width completely contacted on one side, isolated in all the other three sides, and contacted in a circular area with a radius of 9 nm at the tip electrode distance used for each measurement. This radius was approximated with the Hertz model (see SI1) as the maximum contact radius in our measurements. In this geometry we obtain the voltage distribution in the layer and the current density at each point. This allowed us to find the relation between the current (I), length (L), width (W), applied voltage (V) and conductance (σ) in this specific geometry by using the expression $I = \frac{\sigma VW}{L}$. We observe that $I/\sigma V$ is a constant for each geometry. We can obtain I for various V and σ in the program, and therefore, we can obtain the relation W/L needed for estimating the field effect mobility in our samples for each specific geometry.

Data availability statement

The data that support the findings of this study are available upon reasonable request from the authors.

Acknowledgments

We acknowledge financial support from Ministerio de Ciencia e Investigación through the 'María de Maeztu' Programme for Units of Excellence (Grant No. CEX2018-000805-M) and through Grants PID2019-106268GB-C31, PID2019-109539GB-C43 and Ramón y Cajal fellowship RYC2020-030302-I, the Comunidad Autónoma de Madrid through Grants No. S2018/NMT-4321, S2018/NMT-4511 and SI3-PJI-2021-00479, the Generalitat Valenciana through Programa Prometeo/2021/01, and the Centro de Computación Científica of the Universidad Autónoma de Madrid. X L gratefully acknowledges

the support from NSF ECCS-2130552 and the Welch Foundation via grant F-1662 for sample preparation.

Conflict of interest

The authors declare that they have no conflict of interest.

ORCID iDs

Mohammed Moaied  <https://orcid.org/0000-0002-4504-8572>

Pablo Ares  <https://orcid.org/0000-0001-5905-540X>

Juan José Palacios  <https://orcid.org/0000-0003-2378-0866>

Cristina Gomez-Navarro  <https://orcid.org/0000-0002-5609-3387>

References

- [1] Allain A, Kang J, Banerjee K and Kis A 2015 Electrical contacts to two-dimensional semiconductors *Nat. Mater.* **14** 1195–205
- [2] Shen P-C *et al* 2021 Ultralow contact resistance between semimetal and monolayer semiconductors *Nature* **593** 211–7
- [3] Li N *et al* 2020 Large-scale flexible and transparent electronics based on monolayer molybdenum disulfide field-effect transistors *Nat. Electron.* **3** 711–7
- [4] Singh E, Singh P, Kim K S, Yeom G Y and Nalwa H S 2019 Flexible molybdenum disulfide (MoS₂) atomic layers for wearable electronics and optoelectronics *ACS Appl. Mater. Interfaces* **11** 11061–105
- [5] Das S, Chen H-Y, Penumatcha A V and Appenzeller J 2013 High performance multilayer MoS₂ transistors with scandium contacts *Nano Lett.* **13** 100–5
- [6] Liu H, Si M, Deng Y, Neal A T, Du Y, Najmaei S, Ajayan P M, Lou J and Ye P D 2014 Switching mechanism in single-layer molybdenum disulfide transistors: an insight into current flow across Schottky barriers *ACS Nano* **8** 1031–8
- [7] Liu W, Kang J, Cao W, Sarkar D, Khatami Y, Jena D and Banerjee K 2013 High-performance few-layer-MoS₂ field-effect-transistor with record low contact-resistance 2013 *IEEE Int. Electron Devices Meeting* pp 19.4.1–4
- [8] Kang J, Liu W and Banerjee K 2014 High-performance MoS₂ transistors with low-resistance molybdenum contacts *Appl. Phys. Lett.* **104** 093106
- [9] Liu Y *et al* 2015 Toward barrier free contact to molybdenum disulfide using graphene electrodes *Nano Lett.* **15** 3030–4
- [10] Hong W, Shim G W, Yang S Y, Jung D Y and Choi S-Y 2019 Improved electrical contact properties of MoS₂-graphene lateral heterostructure *Adv. Funct. Mater.* **29** 1807550
- [11] Byun K-E *et al* 2013 Graphene for true ohmic contact at metal–semiconductor junctions *Nano Lett.* **13** 4001–5
- [12] Kwak J Y, Hwang J, Calderon B, Alsaman H, Munoz N, Schutter B and Spencer M G 2014 Electrical characteristics of multilayer MoS₂ FET's with MoS₂/graphene heterojunction contacts *Nano Lett.* **14** 4511–6
- [13] Kim T, Fan S, Lee S, Joo M-K and Lee Y H 2020 High-mobility junction field-effect transistor via graphene/MoS₂ heterointerface *Sci. Rep.* **10** 13101
- [14] Singh A K, Hwang C and Eom J 2016 Low-voltage and high-performance multilayer MoS₂ field-effect transistors with graphene electrodes *ACS Appl. Mater. Interfaces* **8** 34699–705
- [15] Kappera R, Voiry D, Yalcin S E, Branch B, Gupta G, Mohite A D and Chhowalla M 2014 Phase-engineered low-resistance contacts for ultrathin MoS₂ transistors *Nat. Mater.* **13** 1128–34
- [16] Kappera R *et al* 2014 Metallic 1T phase source/drain electrodes for field effect transistors from chemical vapor deposited MoS₂ *APL Mater.* **2** 092516
- [17] Lim C H Y X, Nesladek M and Loh K P 2014 Observing high-pressure chemistry in graphene bubbles *Angew. Chem., Int. Ed.* **53** 215–9
- [18] Wang L, Williams C M, Boutilier M S H, Kidambi P R and Karnik R 2017 Single-layer graphene membranes withstand ultrahigh applied pressure *Nano Lett.* **17** 3081–8
- [19] Bandaru N, Kumar R S, Sneed D, Tschauer O, Baker J, Antonio D, Luo S-N, Hartmann T, Zhao Y and Venkat R 2014 Effect of pressure and temperature on structural stability of MoS₂ *J. Phys. Chem. C* **118** 3230–5
- [20] Fan X, Singh J D, Jiang Q and Zheng T W 2016 Pressure evolution of the potential barriers of phase transition of MoS₂, MoSe₂ and MoTe₂ *Phys. Chem. Chem. Phys.* **18** 12080–5
- [21] Zhu S-H, Yan B-L, Zeng W, Fan D-H, Tang B, Liu F-S, Liu X, Qin H, Liu Q-J and New A 2019 Criterion for the prediction of solid-state phase transition in TMDs *Phys. Chem. Chem. Phys.* **21** 24070–6
- [22] Hromádová L, Martoňák R and Tosatti E 2013 Structure change, layer sliding, and metallization in high-pressure MoS₂ *Phys. Rev. B* **87** 144105
- [23] Wu H, Liu X, Yin J, Zhou J and Guo W 2016 Tunable electrical performance of few-layered black phosphorus by strain *Small* **12** 5276–80
- [24] Fu D, Zhou J, Tongay S, Liu K, Fan W, King Liu T-J and Wu J 2013 Mechanically modulated tunneling resistance in monolayer MoS₂ *Appl. Phys. Lett.* **103** 183105
- [25] Quereda J, Palacios J J, Agrait N, Castellanos-Gomez A and Rubio-Bollinger G 2017 Strain engineering of Schottky barriers in single- and few-layer MoS₂ vertical devices *2D Mater.* **4** 021006
- [26] Castellanos-Gomez A, Roldán R, Cappelluti E, Buscema M, Guinea F, van der Zant H S J and Steele G A 2013 Local strain engineering in atomically thin MoS₂ *Nano Lett.* **13** 5361–6
- [27] Ares P, Pisarra M, Segovia P, Díaz C, Martín F, Michel E G, Zamora F, Gómez-Navarro C and Gómez-Herrero J 2019 Tunable graphene electronics with local ultrahigh pressure *Adv. Funct. Mater.* **29** 1806715
- [28] Manzaneres-Negro Y, Ares P, Jaafar M, López-Polín G, Gómez-Navarro C and Gómez-Herrero J 2020 Improved graphene blisters by ultrahigh pressure sealing *ACS Appl. Mater. Interfaces* **12** 37750–6
- [29] Castellanos-Gomez A, Buscema M, Molenaar R, Singh V, Janssen L, van der Zant H S J and Steele G A 2014 Deterministic transfer of two-dimensional materials by all-dry viscoelastic stamping *2D Mater.* **1** 011002
- [30] Ottaviano L *et al* 2017 Mechanical exfoliation and layer number identification of MoS₂ revisited *2D Mater.* **4** 045013
- [31] Horcas I, Fernández R, Gómez-Rodríguez J M, Colchero J, Gómez-Herrero J and Baro A M 2007 WSXM: a software for scanning probe microscopy and a tool for nanotechnology *Rev. Sci. Instrum.* **78** 013705
- [32] BudgetSensors 2022 All-in-one-DD AFM Probe (available at: www.budgetsensors.com/multipurpose-afm-probe-conductive-diamond-all-in-one-dd) (Accessed 19 April 2022)
- [33] Johnson K L 1987 *Contact Mechanics* (Cambridge: Cambridge University Press)
- [34] de Araújo D B, Almeida R Q, Gadelha A C, Rezende N P, Salomão F C C S, Silva F W N, Campos L C and Barros E B 2020 Controlling the electronic bands of a 2D semiconductor by force microscopy *2D Mater.* **7** 045029
- [35] Chaudhary P, Lu H, Loes M, Lipatov A, Sinitskii A and Gruverman A 2022 Mechanical stress modulation of resistance in MoS₂ junctions *Nano Lett.* **22** 1047–52

- [36] Chi Z-H, Zhao X-M, Zhang H, Goncharov A F, Lobanov S S, Kagayama T, Sakata M and Chen X-J 2014 Pressure-induced metallization of molybdenum disulfide *Phys. Rev. Lett.* **113** 036802
- [37] Nayak A P, Bhattacharyya S, Zhu J, Liu J, Wu X, Pandey T, Jin C, Singh A K, Akinwande D and Lin J-F 2014 Pressure-induced semiconducting to metallic transition in multilayered molybdenum disulphide *Nat. Commun.* **5** 3731
- [38] Shimazu Y, Tashiro M, Sonobe S and Takahashi M 2016 Environmental effects on hysteresis of transfer characteristics in molybdenum disulfide field-effect transistors *Sci. Rep.* **6** 30084
- [39] Andrews K, Bowman A, Rijal U, Chen P-Y and Zhou Z 2020 Improved contacts and device performance in MoS₂ transistors using a 2D semiconductor interlayer *ACS Nano* **14** 6232–41
- [40] Bang S *et al* 2020 Contact engineering of layered MoS₂ via chemically dipping treatments *Adv. Funct. Mater.* **30** 2000250
- [41] Andleeb S, Eom J, Naz N R and Singh A K 2017 MoS₂ field-effect transistor with graphene contacts *J. Mater. Chem. C* **5** 8308–14
- [42] Sharma D, Motayed A, Shah P B, Amani M, Georgieva M, Glen Birdwell A, Dubey M, Li Q and Davydov A V 2015 Transfer characteristics and low-frequency noise in single- and multi-layer MoS₂ field-effect transistors *Appl. Phys. Lett.* **107** 162102
- [43] Liu W, Sarkar D, Kang J, Cao W and Banerjee K 2015 Impact of contact on the operation and performance of back-gated monolayer MoS₂ field-effect-transistors *ACS Nano* **9** 7904–12
- [44] Hohenberg P and Kohn W 1964 Inhomogeneous electron gas *Phys. Rev.* **136** B864–71
- [45] Kohn W and Sham L J 1965 Self-consistent equations including exchange and correlation effects *Phys. Rev.* **140** A1133–8
- [46] Ordejón P, Artacho E and Soler J M 1996 Self-consistent order density-functional calculations for very large systems *Phys. Rev. B* **53** R10441–4
- [47] Soler J M, Artacho E, Gale J D, García A, Junquera J, Ordejón P and Sánchez-Portal D 2002 The SIESTA method for *ab initio* order-N materials simulation *J. Phys.: Condens. Matter* **14** 2745–79
- [48] Cooper V R 2010 Van Der Waals density functional: an appropriate exchange functional *Phys. Rev. B* **81** 161104
- [49] Junquera J, Paz Ó, Sánchez-Portal D and Artacho E 2001 Numerical atomic orbitals for linear-scaling calculations *Phys. Rev. B* **64** 235111
- [50] Jacob D and Palacios J J 2011 Critical comparison of electrode models in density functional theory based quantum transport calculations *J. Chem. Phys.* **134** 044118
- [51] Ozaki T 2003 Variationally optimized atomic orbitals for large-scale electronic structures *Phys. Rev. B* **67** 155108
- [52] Ozaki T and Kino H 2004 Numerical atomic basis orbitals from H to Kr *Phys. Rev. B* **69** 195113
- [53] Ozaki T and Kino H 2005 Efficient projector expansion for the *ab initio* LCAO method *Phys. Rev. B* **72** 045121
- [54] Perdew J P, Burke K and Ernzerhof M 1997 Generalized gradient approximation made simple [Phys. Rev. Lett. 77, 3865 (1996)] *Phys. Rev. Lett.* **78** 1396